IEEE Access
Multidisciplinary | Rapid Review | Open Access Journal

Received December 21, 2020, accepted January 4, 2021, date of publication January 13, 2021, date of current version February 5, 2021.

Digital Object Identifier 10.1109/ACCESS.2021.3051339

Intelligent Modeling and Design of a Novel Temperature Control System for a Cantilever-Based Gas-Sensitive Material Analyzer

TIANHAI LU[1], CHAO FEI[1], LIN XUAN[1], HAITAO YU[2], DACHENG XU[1], AND XINXIN LI[2]

[1]School of Electronic and Information Engineering, Soochow University, Suzhou 251000, China
[2]State Key Laboratory of Transducer Technology, Shanghai Institute of Microsystem and Information Technology, Chinese Academy of Sciences, Shanghai 200050, China

Corresponding author: Dacheng Xu (xudacheng@suda.edu.cn)

This work was supported in part by the NSF of China under Grant 61527818 and Grant 61834007.

ABSTRACT Devices used to set and control the environmental temperature are critical to the performance of gas-sensitive material analyzers, which use silicon microcantilevers to characterize the gas-sensitive materials. This paper describes a novel microtemperature-control device that uses a double Peltier structure to replace the traditional refrigerant temperature control system. A proportional-integral-derivative (PID) algorithm is used to achieve accurate and fast temperature control, with a long short-term memory (LSTM) network trained to identify the nonlinear dynamics of the Peltier system. A neighbor hybrid mean center opposition-based learning particle swarm optimization (NHCOPSO) algorithm is proposed to optimize the PID controller. The LSTM network identification is obviously better than that of previous Peltier system identification methods, and the NHCOPSO algorithm is found to be superior to other improved PSO and evolutionary algorithms on benchmark functions and in PID parameter optimization. Experimental results show that the proposed temperature control device greatly improves the accuracy and efficiency of gas-sensitive material analysis with a temperature control range of -40 to 180°C, a temperature control tolerance within ± 0.05°C, a maximum heating rate of 20°C/min, and a maximum cooling rate of -10°C/min.

INDEX TERMS Gas-sensing material analysis, intelligent system identification, long short-term memory, particle swarm optimization, Peltier temperature control system.

I. INTRODUCTION

As microelectromechanical system (MEMS) technology continues to be improved, the applications of silicon microcantilevers in gas-sensing material performance analysis are expanding [1], [2]. In such systems, temperature control of the cantilever directly affects the accuracy of the analysis. Traditional temperature control uses a mechanical refrigerant device to control the cantilever. Reference [3] used resistance wire heating and water bath cooling to control the environmental temperature in an experiment to evaluate the sensitivity of an SnO_2/rgo-4 composite to NO_2. However, in this system, the resistance wire heating had poor accuracy (± 1°C), and the water bath had a low cooling speed (3°C/min). In reference [4], a cantilever-based gas sensor was placed in a water bath temperature-control device to perform experiments to quantitatively calculate material thermodynamic parameters. Although the volume of the whole system was reduced, the temperature of the test environment changed slowly within a small range. In references [5]–[7], a silicon microcantilever-based gas-sensitive material with a temperature range of -50 to 150°C and uniformity of 2°C was developed using liquid nitrogen refrigeration and blast heating. However, the instrument had a large volume ($1100 \times 850 \times 1740$ mm), a low temperature change speed (3°C/min), and poor temperature control accuracy (± 2.5°C); furthermore, maintenance of the liquid nitrogen refrigeration system was both difficult and costly.

The associate editor coordinating the review of this manuscript and approving it for publication was Xiangtao Li.

In short, according to the abovementioned literature, current temperature control systems suffer from large volumes, low temperature change speeds, and poor temperature control sensitivity.

With the development of semiconductor refrigeration technology, temperature control devices based on thermoelectric Peltier coolers have been increasingly used in applications such as MEMS devices [8], medical instruments [9], optical experiments [10], and microscope-sample temperature control [11]. This paper describes the development of a Peltier temperature control device for a microcantilever-based analyzer that can characterize gas-sensitive materials. The proposed device greatly improves the accuracy and efficiency of gas-sensing material evaluation over existing devices. However, due to the nonlinear characteristics of Peltier temperature control devices, it is difficult to accurately construct a mathematical model to analyze and control the system [12]. For example, tuning the parameters of proportional-integral-derivative (PID) controllers based on trial and error [13], [14] results in poor control performance and is very time-consuming. Therefore, to obtain the optimum temperature control effect, it is necessary to optimize the control method and parameters through theoretical analysis or an intelligent algorithm developed based on an accurate Peltier system model. In reference [15], a battery temperature control system based on the Peltier model was regarded as a first-order linear time-invariant system, and the parameters were analyzed experimentally. Reference [16] analyzed the thermal model of a heating and cooling system composed of a Peltier device, a water container, and a fan radiator. The system models presented in references [15], [16], however, do not have adequate accuracy because they neglect the characteristics of the Peltier model parameters, which vary with temperature. Based on the nonlinear characteristics of Peltier systems, an aluminum box microreactor system model has been theoretically analyzed [17]. Reference [18] derived a mathematical model for Peltier heat conduction and examined the relationship between the system parameters and temperature through theoretical derivations and experimental analysis. In reference [19], an analytical method for a thermoelectric refrigeration system that includes the Peltier effect and the Seebeck effect was proposed. Although the three references mentioned above proposed nonlinear Peltier model analysis methods, it is still difficult to quickly and accurately establish the complex structure of a semiconductor temperature control system model [16].

With the development of neural networks, various network structures have been employed for nonlinear system identification. This is because neural networks can perform excellent nonlinear function approximation [20] through the Hopfield [21], radial basis function (RBF) [22], back propagation (BP) [23], nonlinear autoregression with external input (NARX) [24], and broad learning system (BLS) [25] methods. In particular, long short-term memory (LSTM) networks can expertly solve complex nonlinear engineering problems through their powerful learning ability with regard to time series, [26]–[28]. However, LSTM has rarely been applied to Peltier temperature control system model construction. Therefore, this study develops an intelligent and accurate identification method for a Peltier temperature control system based on an LSTM network, thus eliminating the requirement of knowing the thermodynamic and physical states of the system. After establishing the ''black box'' model of the system through an LSTM network, evolutionary algorithms are used to search for the optimal PID control parameters of the system. Here, we consider the artificial sheep algorithm (ASA) [29], particle swarm optimization (PSO) [30], [31], genetic algorithm (GA) [32], and fruit-fly optimization algorithm (FOA) [33]. Compared with other evolutionary methods, PSO can generate high-quality solutions quickly and has more stable convergence characteristics [34]. However, in most PID parameter optimization problems, the search range can be reduced experimentally or through experience, so the optimal solution may be missed. Moreover, a large-scale parameter search can lead to the algorithm becoming trapped around a local optimum, so the PSO method must have strong global convergence. By analyzing some PSO improvement strategies, neighbor hybrid mean center opposition-based learning particle swarm optimization (NHCOPSO) is developed. This technique improves the temperature control precision and speed of a silicon microcantilever-based gas-sensitive material analyzer by identifying the optimum PID control parameters quickly and accurately over a large range.

The remainder of this paper is organized as follows. Section II introduces some theoretical foundations, including the relationship between the performance characterization of gas-sensing materials and the cantilever temperature and the thermal models of existing Peltier devices. Section III describes the structure of a temperature control device based on the Peltier effect and analyzes the complexity of the associated heat conduction model. Section IV discusses how the LSTM network can be applied to Peltier temperature control system identification and compares it with some other methods. Section V describes the basics of the NHCOPSO algorithm and compares its performance with that of other improved PSO and evolutionary algorithms. Experimental results of the silicon cantilever-based gas-sensing material characterization temperature control device designed through the above methods are presented in section VI. Finally, section VII summarizes this paper.

II. THEORETICAL BASIS OF THE SYSTEM DESIGN

A. EFFECT OF THE TEMPERATURE CHANGE OF THE MICROCANTILEVER ON CHARACTERIZATION OF GAS SENSING MATERIALS

Reference [4] describes the conversion of the adsorption and desorption of gas molecules onto a gas-sensing material into changes in the resonant frequency of the cantilever, which enables the calculation of key dynamic/thermodynamic parameters of gas-sensitive materials, such as the enthalpy change ΔH, entropy change ΔS, Gibbs free energy G, and Langmuir equilibrium constant K. Based on this

derivation [4], the present paper mainly analyzes the relationship between the enthalpy change of the gas-sensing material performance parameters and the experimental temperature deviation.

It is assumed that the two temperatures used in the variable temperature weighting method are T_1 and T_2. The corresponding partial pressures of the experimental gases are p_1 and p_2. The gas constant is R. According to reference [4], the enthalpy change ΔH is expressed as:

$$\Delta H = \frac{RT_2T_1}{T_2 - T_1} \ln \frac{p_2}{p_1} \tag{1}$$

The temperature deviation is assumed to be caused by temperature fluctuations or a temperature gradient in the experiment, where the real temperature values are $T_1 + \Delta T_1$ and $T_2 + \Delta T_2$. The enthalpy change $\Delta H'$ given this error is:

$$\Delta H' = \frac{R(T_2 + \Delta T_2)(T_1 + \Delta T_1)}{T_2 - T_1 + \Delta T_2 - \Delta T_1} ln \frac{p_2}{p_1} \tag{2}$$

The error multiple E is expressed as:

$$E = \frac{\Delta H'}{\Delta H} = \frac{(T_2 + \Delta T_2)(T_1 + \Delta T_1)(T_2 - T_1)}{T_1T_2(T_2 - T_1 + \Delta T_2 - \Delta T_1)} \tag{3}$$

Let ΔT_1 and ΔT_2 in (3) be independent variables, let E be the dependent variable, and set the other parameters as constants. The derivatives of ΔT_1 and ΔT_2 can be used to obtain $E_{\Delta T_1}$ and $E_{\Delta T_2}$ as follows:

$$\begin{cases} E_{\Delta T_1} = \dfrac{T_1T_2(T_2 - T_1)(T_2 + \Delta T_2)^2}{(T_1T_2(T_2 - T_1 + \Delta T_2 - \Delta T_1))^2} \\ E_{\Delta T_2} = \dfrac{-T_1T_2(T_2 - T_1)(T_1 + \Delta T_1)^2}{(T_1T_2(T_2 - T_1 + \Delta T_2 - \Delta T_1))^2} \end{cases} \tag{4}$$

Taking the temperature control performance of the modified HWS-225L [5]–[7] as an example, the temperature uniformity is ±2°C, and the temperature fluctuation is ±0.5°C. Therefore, $\Delta T_1, \Delta T_2 \in [-2.5, 2.5]$. T_1 and T_2 are experimental ambient temperatures of 303 K and 318 K [6]. When $T_2 > T_1$, we have $E_{\Delta T_1} > 0$ and $E_{\Delta T_2} < 0$. The error multiple E is approximately 1.5, taking into account the limiting cases $\Delta T_1 = 2.5$ and $\Delta T_2 = -2.5$. Thus, the accuracy of the enthalpy change calculation is greatly reduced.

B. PELTIER MODEL ANALYSIS

A Peltier module is a thermoelectric semiconductor cooling module based on the Peltier effect. When an electric current passes through a material that consists of two different types of semiconductors, one experiences a cooling effect because the charge carriers release excess energy as they move from a high energy level to a low energy level. The other semiconductor experiences a heating effect when the charge carriers move from a low energy level to a high energy level and absorb energy from outside the system.

Peltier's model structure diagram is shown in Fig. 1. It is composed of p-type and n-type thermocouples connected in series by a guide vane with high conductivity. Peltier devices can cool and head due to their PN junction structures, which

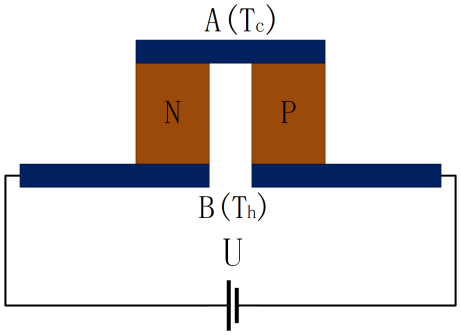

FIGURE 1. Structure of a Peltier module. Voltage U is applied to the Peltier module, and current flows through the n-type and p-type semiconductors. T_c and T_h are the temperatures of the cold side and hot side, respectively.

have nonlinear volt-ampere characteristics. When a current flows through the circuit, heat will be absorbed at connector A and released at connector B so that $T_h > T_c$. Therefore, the temperature difference between A and B is $\Delta T = T_h - T_c$.

In practice, when a voltage U is applied to a Peltier element, the Peltier effect, heat conduction, and Joule heat will occur at the junction between the hot and cold ends. Therefore, the heat Q_c absorbed by the cold side can be expressed as:

$$Q_c = \alpha T_c I - \frac{1}{2} I^2 R - \frac{\kappa S}{H}(T_h - T_c) \tag{5}$$

In (5), α, I, R, κ, S, and H denote the Seebeck effect factor, the current flowing through the Peltier element, the resistance value of the device, the total thermal conductivity of the device, and the cross-sectional area and length of the p-type or n-type semiconductors in the device, respectively. The first term on the right-hand side of (5) represents the Peltier effect. The second term is the Joule heat. As the Joule heat is divided into both the cold and hot sides, only half of the Joule heat is considered in the calculation. The third term represents the heat conduction between the hot and cold sides resulting from the temperature difference. Similarly, the heat Q_h released from the hot side is expressed as:

$$Q_h = \alpha T_h I + \frac{1}{2} I^2 R - \frac{\kappa S}{H}(T_h - T_c) \tag{6}$$

Due to the inhomogeneity of the materials, the parameters α, R, and κ in (5) and (6) often change with temperature. These variations can be written as:

$$\alpha = \frac{U}{T_h} \tag{7}$$

$$R = \frac{U}{I}\left(1 - \frac{(T_h - T_c)}{T_h}\right) \tag{8}$$

$$\kappa = \frac{HUIT_c}{2ST_h(T_h - T_c)} \tag{9}$$

Once the temperature of the Peltier element's cold and hot sides has been determined, the relationships between α, R, κ, and temperature become linear, and the associated expressions can be determined experimentally [18]. However, the temperature of the hot and cold surfaces in the Peltier system is not constant, and it is difficult to confirm its precise value, so the above relationship is impossible to obtain.

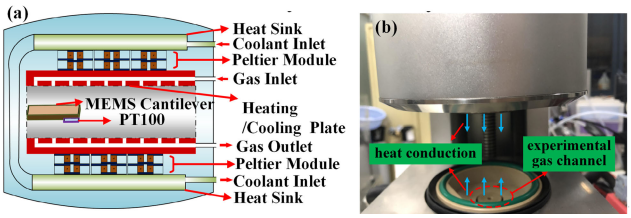

FIGURE 2. Structure of temperature control chamber. (a) Structural schematic diagram of the cantilever-based gas-sensitive material analyzer. (b) Photograph of the experimental cavity.

III. STRUCTURE AND MODEL OF THE TEMPERATURE CONTROL SYSTEM

A. STRUCTURE OF THE TEMPERATURE CONTROL SYSTEM

Based on the relationship between the characteristic parameters of a gas-sensing material and the environmental temperature and on an analysis of the Peltier device thermal model, a miniaturized cavity based on a double-layer Peltier structure is proposed. The structure and the physical object are shown in Fig. 2.

The temperature control chamber includes five main parts.

(a) Peltier modules are placed on the upper and lower sides of the chamber to control the temperature of the test environment through the heat transfer between the cavity wall and the gas in the chamber. The shape of the cavity is a cylinder with a height of 2 cm and a bottom radius of 3 cm. The small volume of the cavity accelerates the temperature change around the cantilever-based gas sensor.

(b) The Peltier elements on either side have a double-layer structure. The outer Peltier element acts as a heat sink for the inner Peltier element and exchanges heat with the circulating liquid cooling device. The working state of the inner Peltier element is controlled by the circuit to regulate the temperature. The inner components are TEC1-3505 and TEC1-3506 modules, while the outer component is a TEC1-3506 module. The maximum temperature difference is approximately 75°C. Therefore, the temperature range of the device can be extended to −40 to 180°C by the double-layer structure.

(c) The cooling system uses the circulating liquid provided by a thermostatic bath for heat exchange.

(d) At the top and bottom, the wall of the chamber is connected with an external conduit to introduce and discharge the experimental gas, respectively.

(e) The structure of the temperature control system is shown in Fig. 3. The temperature is detected by a PT100 device near the cantilever-based gas sensor, and the platinum resistance signal is converted into a voltage signal by a signal processing circuit before being transmitted to a microcontroller unit (MCU) through an analog-to-digital converter (ADC). According to the current temperature value, the MCU calculates and outputs the corresponding duty cycle of the pulse width modulation (PWM) signal as the control signal. Using the power isolation circuit and the driving circuit, the Peltier system's working power is finally regulated to achieve temperature control.

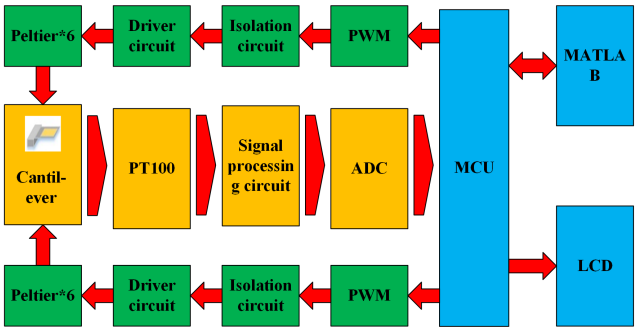

FIGURE 3. Flowchart of temperature control system.

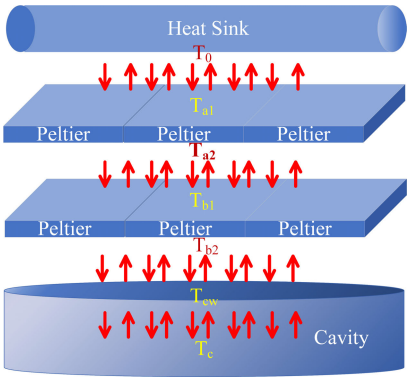

FIGURE 4. Peltier heat conduction structure diagram. Heat is transferred between five layers, namely, a heat sink, an outer Peltier element, an inner Peltier element, the cavity wall, and the gas around the cantilever.

B. MODEL ANALYSIS OF THE PELTIER TEMPERATURE CONTROL SYSTEM

Although a thermal model of the Peltier module was presented and the relationship between the parameters of a Peltier device and the temperature was analyzed in section II, the specific temperature of the cold and hot sides of the device cannot be determined in practical applications. It is impossible to accurately establish the dynamic model of a Peltier system in the process of temperature control using the method described in reference [18].

The detailed components of the Peltier heating/cooling parts (see Fig. 2) are shown in Fig. 4. The temperature control structure is divided into four parts, including a radiator filled with circulating liquid provided by an external water tank with a constant temperature of T_0; a Peltier layer for heat dissipation, whose outer temperature is T_{a1} and internal temperature is T_{a2}; a Peltier element used for heating/cooling, whose outer temperature is T_{b1} and internal temperature is T_{b2}; and a cavity wall with a temperature of T_{cw}. The external environment has a temperature of T_c.

The actual temperature control process consists of four heat exchange processes: (i) between the radiator and the Peltier element; (ii) between the Peltier element for heat dissipation and the Peltier element of the heating/cooling layer; (iii) between the Peltier element of the heating/cooling layer and the wall of the experimental chamber; and (iv) between the cavity wall and the internal gas environment. It is difficult

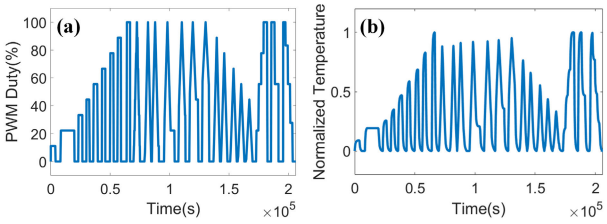

FIGURE 5. System identification training data. (a) Sequence input to an actual Peltier temperature control device. (b) Sequence output from an actual Peltier temperature control device.

to derive the temperature model for the whole system through theoretical analysis and calculations, because the temperature inside and outside the Peltier system cannot be accurately determined.

IV. SYSTEM IDENTIFICATION BASED ON AN LSTM NETWORK

A. BASIS OF SYSTEM IDENTIFICATION

System identification refers to the process of determining an equivalent model that can describe the actual system characteristics from many given models based on existing input and output data from the system [39]. The advantage of this method is that the system model can be obtained using only input and output data from the system. The main process includes system data acquisition, system model establishment, and model parameter identification.

Because of the differences between the heating and cooling stages of the temperature control system, it is necessary to identify models for the heating and cooling stages independently. This paper mainly examines system identification based on an LSTM network, taking the heating stage as an example. The input to the Peltier temperature control system designed in this paper is a PWM signal ($0-100\%$) with different duty cycles calculated by the MCU, and the output is the temperature value detected by the PT100 near the cantilever-based gas sensor. There is a delay between the input and output data due to the heat transfer through the two Peltier layers, the cavity wall, and the internal gas environment. Thus, it is difficult to accurately represent the system characteristics from random input signal data. According to the law of temperature change in the process of temperature control, the following groups of data are selected for system identification: step response, increasing response, and decreasing response. To facilitate the follow-up tests, the starting temperature of each group of identification data is set to 24°C, and the system returns to the initial state without input after the test. As the system is in the initial state (∼24°C) at the beginning and end of each test, a series of 206218 samples is obtained by connecting each group of data end-to-end. Fig. 5 shows the input and output sequences of the system identification training data.

To compare the identification capabilities of various methods, we also collected three basic test sets and three control test sets. The system input and output sequences of basic sets test1–test3 and control sets test4–test6 are shown in Fig. 6.

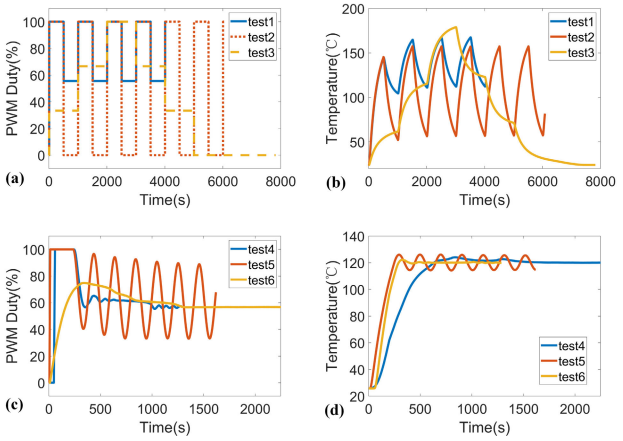

FIGURE 6. System identification test data. (a) Sequence input to an actual Peltier temperature control device in test 1–test 3. (b) Sequence output from an actual Peltier temperature control device in test 1–test 3. (c) Sequence input to the actual Peltier temperature control device in test 4–test 6. (d) Sequence output from the actual Peltier temperature control device in test 4–test 6.

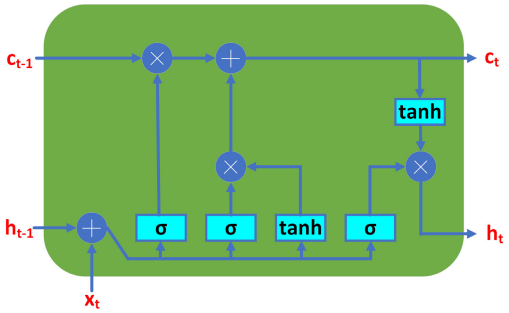

FIGURE 7. Structure of an LSTM cell with forget gate, input gate, and output gate.

The control test sets represent the input and output sequences obtained in the process of controlling the system with PID parameters

$$\begin{cases} k_p = 30 \\ k_i = 0.2 \\ k_d = 100, \end{cases} \quad \begin{cases} k_p = 61 \\ k_i = 4.7 \\ k_d = 0, \end{cases} \quad \text{and} \quad \begin{cases} k_p = 150 \\ k_i = 3.7 \\ k_d = 0. \end{cases}$$

B. LSTM NETWORK

A recurrent neural network (RNN) is an improved artificial neural network that includes hidden layers with self-feedback. Compared with general fully connected neural networks, RNNs have several advantages when dealing with time series problems because of their short-term memory ability. However, the traditional RNN is prone to gradient explosion and gradient disappearance during iteration processes with very long time series [26]. The LSTM network is an improved RNN based on gate control. When processing information at time t in the time series, the internal state c_t is input for the transmission of circular information, and the external state h_t is output. The structure of the LSTM network is shown in Fig. 7.

The three gates in the LSTM structure are a forget gate f_t, an input gate i_t, and an output gate o_t. The forget gate controls how much information needs to be forgotten by the internal state c_{t-1} from the previous time step. The input gate controls how much information needs to be saved for the candidate state $\tilde{c}_t$ at the current time step. The output gate controls how much information needs to be output to the external state h_t of the internal state c_t at the current time step. The update equations for the three gates are as follows:

$$i_t = \sigma(W_i x_t + U_i h_{t-1} + b_i) \tag{10}$$
$$f_t = \sigma(W_f x_t + U_f h_{t-1} + b_f) \tag{11}$$
$$o_t = \sigma(W_o x_t + U_o h_{t-1} + b_o) \tag{12}$$

where x_t is the input of the LSTM unit at time t and h_{t-1} is the external state at the last time step. Candidate state $\tilde{c}_t$, internal state c_t, and external state h_t are calculated by the following equations:

$$\tilde{c}_t = tanh(W_c x_t + U_c h_{t-1} + b_c) \tag{13}$$
$$c_t = f_t \odot c_{t-1} + i_t \odot \tilde{c}_t \tag{14}$$
$$h_t = o_t \odot tan(c_t) \tag{15}$$

The output sequence of a fully connected layer is often added after the LSTM unit, and its expression is as follows:

$$y_t = ReLU(W_{fc2}(ReLU(W_{fc1} h_t + b_{fc1})) + b_{fc2}) \tag{16}$$

where W_i, U_i, b_i, W_f, U_f, b_f, W_o, U_o, b_o, W_c, U_c, *and* b_c in (10)–(15) are the weights of the LSTM cell, and W_{fc1}, W_{fc2}, b_{fc1}, *and* b_{fc2} in (16) represent the weights of the two fully connected layers. The activation functions $\sigma(x)$, $tanh(x)$, and $ReLU(x)$ are calculated as follows:

$$\sigma(x) = \frac{1}{1 + e^{-x}} \tag{17}$$
$$tanh(x) = \frac{e^{x} - e^{-x}}{e^{x} + e^{-x}} \tag{18}$$
$$ReLU(x) = \begin{cases} 0, & x < 0 \\ x, & x \geq 0 \end{cases} \tag{19}$$

C. SYSTEM IDENTIFICATION BASED ON AN LSTM NETWORK

This paper proposes a method of model identification for the Peltier temperature control system based on an LSTM network. A flowchart of the proposed approach is shown in Fig. 8. First, a network is constructed with an LSTM layer containing 25 hidden nodes, one 25 × 12 fully connected (FC) layer and one 12 × 1 fully connected layer, and an ReLU layer. The mean square error (MSE) of a loss function and the Adam optimization method [27] are used to train and update all weights in the network. Finally, the trained network is initialized with hidden layer state h_0 and memory unit state c_0, and the current system input sequence is sent to the LSTM network to obtain the system output sequence of the identification model for subsequent analysis.

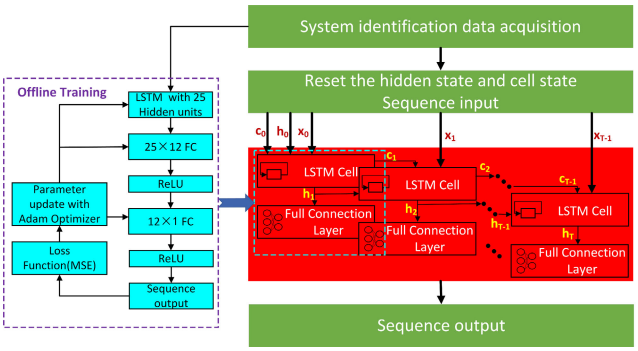

FIGURE 8. Structure of the identification system based on an LSTM network. The "black box" model is obtained by offline training of the LSTM network using the data in Fig. 5. The states of the network are then initialized to process the current system input sequence and output the corresponding sequence.

TABLE 1. Comparison of training results obtained from LSTM networks with different structures.

Model	Number of LSTM layer hidden units	Fitness (%)
LSTM10	10	92.79
LSTM25	25	98.76
LSTM50	50	95.24

To explain the identification process more intuitively, the *fitness* (%) is selected as the identification evaluation criterion. This is calculated as:

$$fitness = 100(1 - \frac{\|ymeasured - ymodel\|_2}{\|ymeasured - \overline{ymeasured}\|_2}) \tag{20}$$

where $y_{measured}$ and $y_{\bar{measured}}$ represent the actual system output sequence and its mean value. y_{model} represents the identification model output sequence, and $\|\cdot\|_2$ denotes the 2-norm calculation. The *fitness* evaluation function reflects the similarity between the output of the identification model and the actual system given the same input sequence. The value of this function has a range of $(-\infty, 100]$, with higher values indicating better system identification performance.

We compared the training results produced by LSTM networks with different numbers of hidden nodes and their performance on basic sets test1–test3. The model with the highest *fitness* value was selected as the final system identification result. LSTM networks with 10, 25, and 50 hidden nodes and two fully connected layers were selected for comparison after training. The final training results and performance on the training sets and the basic test sets are separately presented in Table 1 and Figs. 9–12. The results show that network LSTM25 achieves the best performance in terms of identifying the Peltier temperature control system designed in this paper, as the output curve on the basic test sets is the most similar to that of the practical system.

D. OTHER SYSTEM IDENTIFICATION METHODS

(a) As stated in section I, most Peltier system modeling methods are based on theoretical analysis and system

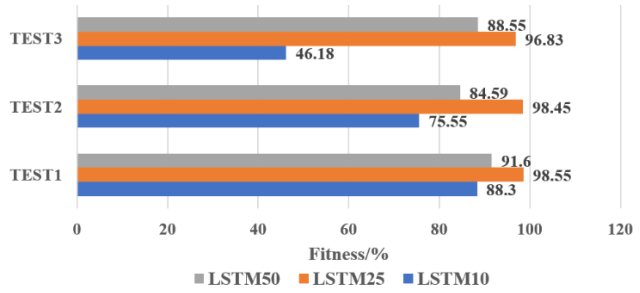

FIGURE 9. Comparison of the performance of networks LSTM10, LSTM25, and LSTM50 on basic test sets.

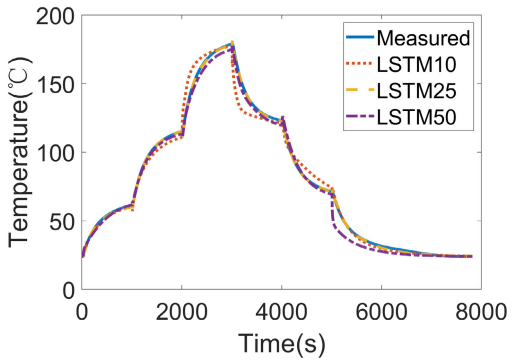

FIGURE 10. Identification results for networks LSTM10, LSTM25. and LSTM50 on test set 1.

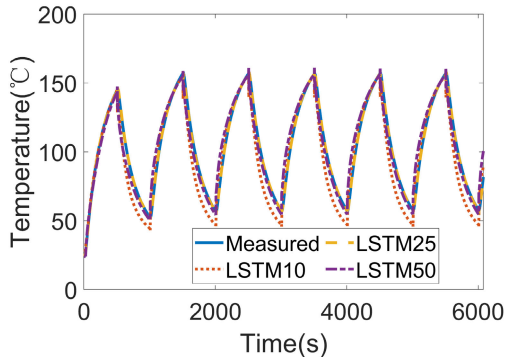

FIGURE 11. Identification results for networks LSTM10, LSTM25, and LSTM50 on test set 2.

identification, with a transfer function used as the simulation model of the whole system. In this study, we used a training sequence of length 206218 and the system identification tool in MATLAB to establish the system model. To obtain the best identification model, 24 transfer functions were constructed based on the common structure shown in Fig. 13, which includes the number of poles (1, 2, 3) and whether there are zero points, delay terms, and integrators. The best model was determined by comparing the performance of all 24 structures on the training sequence and basic sets test1–test3.

(b) NARX was selected as a comparative system identification method [24]. In the literature, the NARX neural network tool in MATLAB has been used to build network structures. We selected the NARX model from MATLAB's

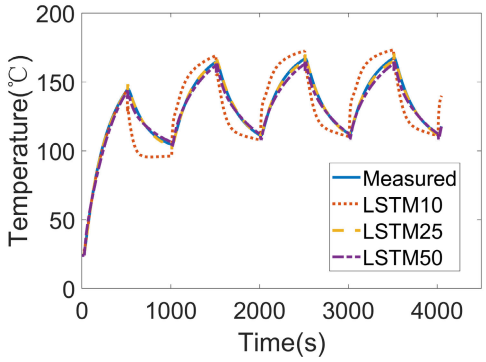

FIGURE 12. Identification results for networks LSTM10, LSTM25, and LSTM50 on test set 3.

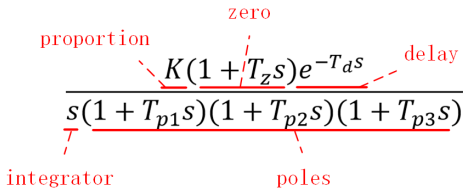

FIGURE 13. Structure of the transfer function model, including proportion, zero, delay, integrator, and poles.

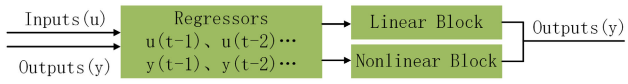

FIGURE 14. Structure of the NARX model, including regressors, a linear block, and a nonlinear block.

system identification tool to identify the system. The resulting structure is shown in Fig. 14. The NARX model takes the system input control variables and system state variables of M moments as the regression factors of the model and then inputs them into the linear and nonlinear modules, respectively, to obtain the output sequence. To obtain the most suitable NARX model for Peltier temperature control system identification, we constructed 12 NARX models by setting the input control delay of the system to 0, 1, 2, or 3 and the parameter M to 1, 2, or 3. The performance of each structure on the training sequence and the basic test sets was then compared.

(c) Theoretically, a three-layer BP neural network is capable of approximating any continuous function. Hence, BP neural networks are often used to identify nonlinear systems [23]. However, BP has no memory function and cannot deal with time series problems accurately. Thus, it is often necessary to take the system state variables of M moments as the current input of the BP network, as in the NARX model. Fig. 15 presents the structure of a three-layer BP neural network, including an input layer, a hidden layer with sigmoid activation function, and an output layer. To obtain the best system identification using a BP neural network, M was set to 1, 2, or 3, and the number of hidden layer nodes was

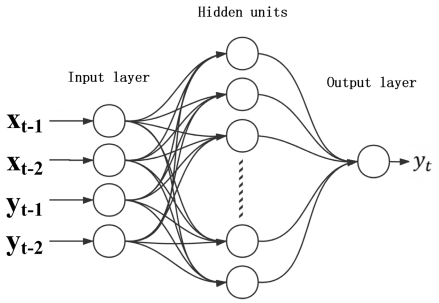

FIGURE 15. Structure of a three-layer BP network model, including the input layer, hidden units, and output layer.

TABLE 2. Identification results using P3Z, NARX1, BP10-2, and LSTM25.

Model	Training sequence	Test 1	Test 2	Test 3
P3Z	54.8%	86.96%	90.92%	71.29%
NARX1	96.59%	95.30%	82.62%	87.28%
BP10-2	95.75%	93.91%	85.97%	88.32%
LSTM25	98.76%	98.55%	98.45%	96.83%

set to 10, 20, or 40. The resulting nine BP network structures were then compared to determine the best model.

Finally, the best identification model was selected from each of the three methods. These were the transfer function model P3Z, with three poles and one zero, the NARX1 model, with an input control delay of 0 and $M = 1$, and BP10-2, with 10 hidden layer nodes and $M = 2$. Their identification results on the training sequence and basic sets test1–test3 are presented in Table 2.

Table 2 indicates that the P3Z model does not provide satisfactory identification performance using the training sequence. This may be because the long sequence contains a large number of system characteristics, including many nonlinear features. Therefore, the model accumulates numerous errors from the continuous input sequence, resulting in poor identification. However, P3Z exhibits good identification performance on basic sets test1–test3 because the short sequence lengths allow little opportunity for error accumulation. In contrast, NARX1 and BP10-2 perform well with both the training sequence and the basic test sets.

E. COMPARISON OF IDENTIFICATION METHODS

The models with the best system identification performance were P3Z, NARX1, BP10-2, and LSTM25. These four models were then compared using a two-step process. First, input sequences consisting of control sets test4–test6 were used as the input to each model, and their output curves were compared with data from the actual system. As shown in Fig. 16, the PID parameters corresponding to control sets test4–test6 were directly used as the PID control parameters of each model, and their response curves were compared. The three groups of tests are named test4ctr, test5ctr, and test6ctr.

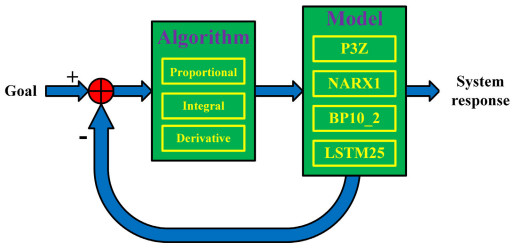

FIGURE 16. Structure of the identification model control test.

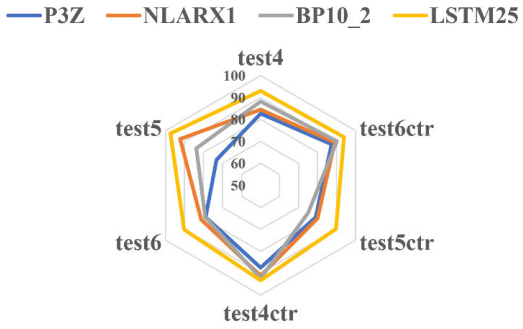

FIGURE 17. Fitness comparison of six tests using the four models.

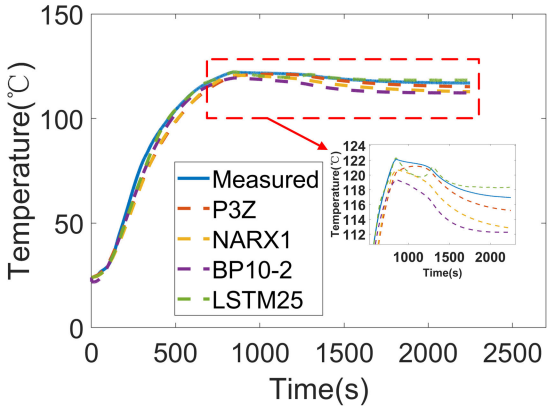

FIGURE 18. Identification results for set test4 using the four models.

Fig. 17 compares the *fitness* values of the four models for tests test4–test6 and test4ctr–test6ctr; the details of each model identification curve for each test are shown in Figs. 18–23. The graphs show the output curves of the four models and of the real system. The system identification performance of LSTM25 is better than that of the other three models for all six groups of tests, simulating the output curve of the system the most accurately. To verify the system identification performance of the LSTM network, the output curve measured by testing the actual system was compared with that given by the LSTM network model in subsequent system control parameter tests.

V. DESIGN OF PID PARAMETER OPTIMIZATION BASED ON NHCOPSO

A. PSO ALGORITHM

PSO is a population-based stochastic optimization technique [42]. It imitates the swarm behavior of insects and herds of animals, birds, and fish as they search for food cooperatively.

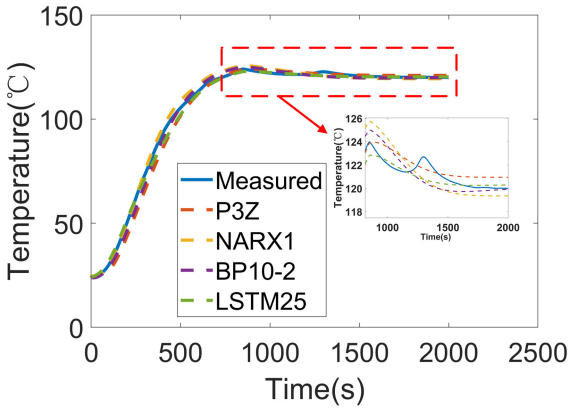

FIGURE 19. Identification results for set test4ctr using the four models.

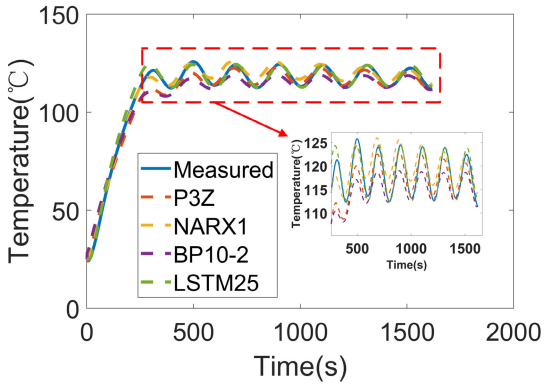

FIGURE 20. Identification results for set test5 using the four models.

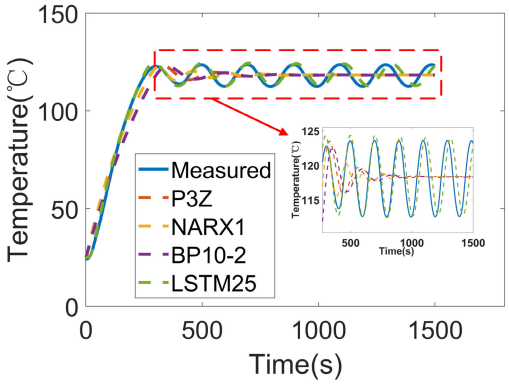

FIGURE 21. Identification results for set test5ctr using the four models.

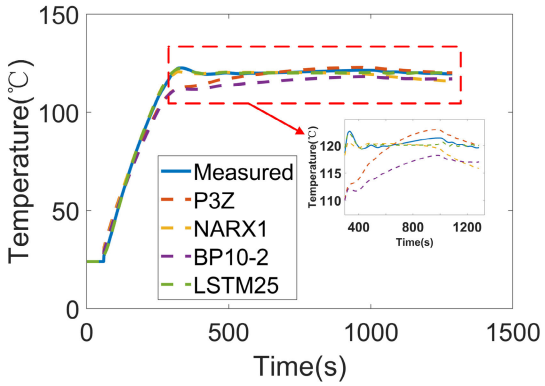

FIGURE 22. Identification results for set test6 using the four models.

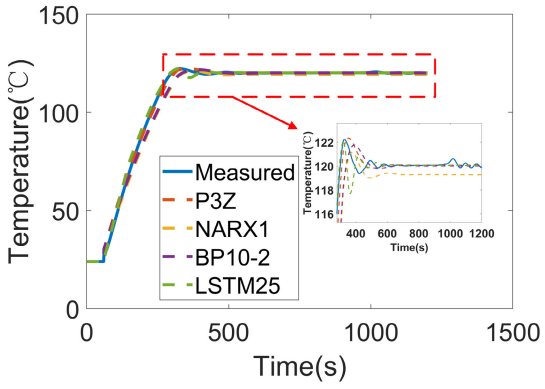

FIGURE 23. Identification results for set test6ctr using the four models.

Each member of the group changes its search mode by learning from its own experience and the experience of other members. The convergence speed of the algorithm is fast, and the calculation is simple and easy to implement. Martingale theory [43] suggests that the PSO algorithm converges to the global optimum with a probability of 1, so PSO has been applied to various optimization problems [34].

However, as the search scope or complexity increases, the PSO algorithm may become trapped around a local extremum. Thus, improved PSO algorithms have become the focus of considerable research. In reference [35], the mean center was used to search the region of interest, and opposition-based learning (OBL) was used to enable particles to explore additional new regions. Reference [36] used a random topology and OBL to improve the global search ability of the algorithm, while reference [37] combined the firefly algorithm with PSO to rapidly find a reliable solution. Reference [38] combined phasor theory with PSO and achieved good results.

In the basic PSO algorithm, problem optimization involves each particle learning its own best position *pbest* and that of the population *gbest*. For a d-dimensional search space problem, suppose that the number of particles in the population is n and the position and velocity of the population are given by $x_i = (x_1^i, x_2^i, \cdots, x_d^i, \cdots, x_D^i)$ and $v_i = (v_1^i, v_2^i, \cdots, v_d^i, \cdots, v_D^i)$, respectively, where $i = 1, 2, \cdots, N$ and $d = 1, 2, \cdots, D$. The positions and velocities are updated according to (21) and (22), where k is the number of iterations, ω is the inertia weight, c_1 and c_1 are learning factors, and r_1 and r_2 are random numbers in the range (0, 1).

$$v_d^{i,k+1} = \omega^* v_d^{i,k} + c_1{}^* r_1{}^* (pbest_d^{i,k} - x_d^{i,k}) + c_2{}^* r_2{}^* (gbest_d^{i,k} - x_d^{i,k}) \quad (21)$$

$$x_d^{i,k+1} = x_d^{i,k} + v_d^{i,k+1} \quad (22)$$

B. THEORY AND STRUCTURE OF NHCOPSO

Although the PID parameter optimization problem for the Peltier temperature control system has only three dimensions, the unknown system model makes it difficult to establish the search range for the control parameters. Therefore, the algorithm needs to search over a large range to ensure optimal control performance. To speed up the convergence of the algorithm in the process of parameter optimization and to prevent the algorithm from becoming trapped around a local optimum, an improved PSO algorithm based on the neighbor hybrid mean center (NHMC) and OBL is designed.

It has been noted [44] that particles in a given neighborhood can interact with each other and search for more regions in the problem space after being divided into several neighborhoods according to a certain topology. Additionally, combined with the partial mean center theory [35], NHMC can replace the neighborhood center of gravity [36] to guide the local particle motion. Reference [36] uses a random topology as the neighborhood structure and found that the convergence was better than that of square and circular topologies. Therefore, in this paper, random topology is used to form a domain j with K particles, find the neighbor hybrid mean center $NHMC_j$ and calculate the reverse position of the particles based on the OBL algorithm.

The mean center NMC_j and local mean fitness are calculated in neighborhood j using:

$$x_{d,j}^{NMC} = \frac{1}{K}\sum_{i=1}^{K} x_{d,j}^{i} \tag{23}$$

$$F_{NM_j} = \frac{1}{K}\sum_{i=1}^{K} fit_j^i \tag{24}$$

where $x_{d,j}^{NMC}$ represents the information on neighborhood mean center NMC_j in each dimension d, fit_j^i represents the fitness value of particle x_j^i in neighborhood j, and $i = 1, 2, \cdots, K$. Particles with fitness values greater than the average F_{NM_j} in neighborhood j are then selected as particle m, where $1 \le m < K$. Each dimension of the neighborhood partial mean center NPC_j can be expressed as:

$$x_{d,j}^{NPC} = \frac{1}{M}\sum_{i=1}^{K} x_{d,j}^{i} \tag{25}$$

In (25), M is the number of particles that have fitness values better than F_{NM_j} in neighborhood j, and d is the dimension. Finally, to better guide the motion of the local particles, the lowest fitness value is selected from among NMC_j, NPC_j, and the lowest fitness value $nbest_j$ in neighborhood j as the neighborhood hybrid mean center point $NHMC_j$:

$$NHMC_j = min(nbest_j, NMC_j, NPC_j) \tag{26}$$

Although NHMC allows the algorithm to quickly identify the optimal local value, the particles may become trapped around a local extremum when the search range is large because of a decrease in population diversity. In the proposed method, OBL is used to evaluate the current solution and its opposite solution at the same time, with the results applied to accelerate the search process [43]. Combined with the method described in this paper, the neighborhood hybrid mean center $NHMC_j$ is used to move particle x_j^i in the opposite direction to obtain $OBLx_j^i$. Suppose that the dynamic boundary $[a_j, b_j]$ of neighborhood j is calculated by the following equation:

$$a_{d,j} = min(x_d^i), \quad b_{d,j} = max(x_d^i) \tag{27}$$

where $a_{d,j}$ and $b_{d,j}$ are the minimum and maximum values of all points in neighborhood j and dimension d. The opposite point position $OBLx_j^i$ is calculated by (28), and each dimension of the opposite point is constrained by (29).

$$OBLx_j^i = 2^*NHMC_j - x_j^i \tag{28}$$

$$OBLx_{d,j}^i = \begin{cases} a_{d,j} + rand * (NHMC_{d,j} - a_{d,j}), \\ \qquad OBLx_{d,j}^i < a_{d,j} \\ NHMC_{d,j} + rand * (b_{d,j} - NHMC_{d,j}), \\ \qquad OBLx_{d,j}^i > b_{d,j} \end{cases} \tag{29}$$

In the above equations, *rand* is a random number in [0, 1], and P is an artificially set threshold. According to the above calculation and analysis, the NHCOPSO algorithm can be divided into three steps. First, the population is initialized, and then the neighborhood structure is constructed randomly. Finally, the hybrid centers of each neighborhood are calculated, and the particles are guided to move. Table 3 describes the details of the algorithm.

TABLE 3. NHCOPSO algorithm.

```
Input: Problem to be optimized
Output: Global optimal particle and its fitness
Function: Find the best solution for the problem
Initialize the population x_i and v_i of
   population size N;
Calculate the fitness of particles f(x_i);
while k ≤ T_max
 if rand < P
      Rebuild particle neighbor matrix;
      Calculate neighborhood hybrid center
       NHMC_j according to (23)–(26);
      for j = 1: N
       for i = 1: K
            Calculate opposite particles OBLx_j^i according to
            (27)–(29);
        if f(OBLx_j^i) < f(x_j^i)
         x_j^i = OBLx_j^i;
        end if
       end for
      end for
 else
      Update the velocity and position of each particle according
      to (21), (22);
 end if
 Update the personal best (pbest) and the global best (gbest);
 k = k + 1;
end while
```

TABLE 4. Results on CEC2013 test functions (D = 30).

Function	OPSO	GOPSO	NCOPSO	HCOPSO	NHCOPSO
f1	2.46E-04	9.36E-04	**2.27E-13**	2.73E-13	5.33E-04
f2	3.26E+07	3.19E+07	**3.65E+06**	4.89E+06	4.29E+06
f3	4.03E+09	6.20E+09	7.28E+07	1.89E+08	**6.59E+07**
f4	3.47E+04	3.49E+04	2.05E+04	1.66E+04	**4.54E+03**
f5	2.74E-02	2.22E-02	2.85E-03	**1.18E-12**	5.48E-02
f6	1.16E+02	1.32E+02	1.08E+02	4.15E+01	**2.99E+01**
f7	1.13E+02	1.16E+02	**2.93E+01**	5.90E+01	3.69E+01
f8	2.10E+01	2.10E+01	2.10E+01	2.10E+01	**2.09E+01**
f9	3.55E+01	3.41E+01	2.34E+01	2.75E+01	**1.84E+01**
f10	1.50E+01	3.73E+01	**2.36E-01**	7.30E-01	7.97E+00
f11	5.74E+01	5.38E+01	6.02E+01	4.23E+01	**3.67E+01**
f12	1.53E+02	1.44E+02	**5.93E+01**	8.39E+01	6.19E+01
f13	2.28E+02	2.31E+02	1.33E+02	1.66E+02	**1.30E+02**
f14	1.63E+03	1.52E+03	6.98E+03	**1.19E+03**	2.02E+03
f15	**4.54E+03**	4.68E+03	6.23E+03	6.12E+03	4.55E+03
f16	2.62E+00	2.46E+00	2.51E+00	2.37E+00	**2.09E+00**
f17	6.59E+01	6.92E+01	1.83E+02	8.26E+01	**6.41E+01**
f18	2.57E+02	2.86E+02	**1.80E+02**	2.43E+02	2.01E+02
f19	5.70E+00	5.61E+00	9.39E+00	3.84E+00	**2.73E+00**
f20	1.47E+01	1.45E+01	1.32E+01	1.22E+01	**1.15E+01**
f21	**2.93E+02**	3.16E+02	3.06E+02	3.11E+02	4.00E+02
f22	1.86E+03	2.04E+03	6.69E+03	**1.18E+03**	2.11E+03
f23	4.87E+03	5.26E+03	7.23E+03	5.62E+03	**3.55E+03**
f24	2.92E+02	2.96E+02	**2.40E+02**	2.74E+02	2.55E+02
f25	3.19E+02	3.20E+02	3.11E+02	**2.91E+02**	3.08E+02
f26	**2.02E+02**	**2.02E+02**	2.74E+02	2.58E+02	3.22E+02
f27	1.22E+03	1.22E+03	**7.14E+02**	9.82E+02	8.57E+02
f28	8.78E+02	1.09E+03	**3.00E+02**	5.99E+02	9.61E+02
Ranks	3.55	3.95	2.77	2.52	2.21

C. COMPARISON OF ALGORITHMS BASED ON CEC2013 FUNCTIONS

Four improved PSO algorithms mentioned in reference [35] were selected as comparative algorithms: opposition-based particle swarm algorithm (OPSO), generalized opposition-based particle swarm algorithm (GOPSO), neighborhood centroid opposition-based particle swarm algorithm (NCOPSO), and hybrid mean center opposition-based learning particle swarm algorithm (HCOPSO). Additionally, the 28-function CEC2013 benchmark was chosen to compare the performance of the algorithms. To ensure the correctness of each algorithm, the optimization results on the 30-dimensional CEC2013 benchmark functions from reference [35] were directly used for the subsequent comparison. The parameters for the NHCOPSO algorithm were set as follows: $\omega = 0.5, c_1 = c_2 = 2, K = 5, N = 30$, and $P = 0.3$. For the other four improved algorithms, the maximum number of evaluations *maxfes* was set to 10^5. Each algorithm was executed independently 25 times on each of the 28 functions, and the mean value was taken as the final result. The experimental results are presented in Table 4.

Compared with the other algorithms, NHCOPSO exhibits superior performance on the optimization functions. The Friedman test was carried out on the optimized results, and NHCOPSO was found to have the best average rank (2.21). This verifies that the overall optimization performance of the NHCOPSO algorithm is better than that of the other four algorithms.

D. COMPARISON OF PID PARAMETER OPTIMIZATION

The black box model obtained by identification of the Peltier-based temperature control system with the LSTM network

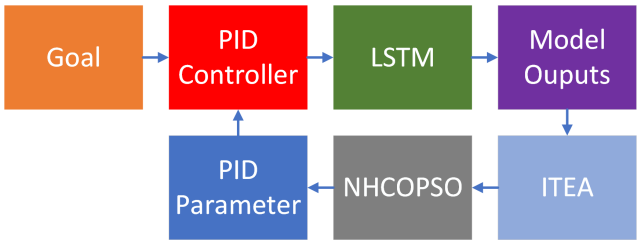

FIGURE 24. PID parameter optimization process.

(see section IV) was used as the control object to optimize the PID parameters. First, the temperature control targets were set to 120°C and 180°C to compare the control parameter optimization results for different temperature points in the same temperature segment. The calculation result $u(k)$ given by (30) was then used to control the black box model. System control performance was evaluated in terms of the integrated time and absolute error (ITAE), which is also used as the fitness function of NHCOPSO. Finally, the PID parameters were identified according to the algorithm in Table 3. A flowchart of this process is shown in Fig. 24.

$$u(t) = K_p e(t) + K_i \sum_{j=0}^{t} e(j) + K_d ec(t) \tag{30}$$

$$ITAE = \int_0^{\infty} t\,|e(t)|\,dt \tag{31}$$

where $e(t)$ is the difference between the system output and the target value, and K_p, K_i, K_d represent the proportional, integral, and differential coefficients of the PID, respectively. The ITAE is used to evaluate the performance of the control system, with smaller values indicating better control performance.

In this study, the ASA [43], PSO [44], and GA [46] methods were used for PID control parameter optimization, and their results were compared with those of NHCOPSO. After several optimization experiments for control parameters in different ranges, we choose a typical set of search scopes as an example to show the algorithm comparison results. The search range was $K_p \in (0, 3000)$, $K_i \in (0, 15)$, $K_d \in (0, 8000)$, and the number of evaluations was set to 10000. The parameters of NHCOPSO were the same as those specified in the previous section; the ASA, PSO, and GA parameters were set according to references [29], [30], and [32], respectively. Table 5 lists the parameter values and control performance of the PID algorithm as optimized by the four algorithms under the target temperature of 180°C. Fig. 25 shows the ITAE convergence curves of the four algorithms during PID parameter optimization under the target temperature of 120°C.

NHCOPSO is obviously superior to the other three algorithms in terms of search speed and precision, rapidly identifying PID control parameters that are more suitable for the system model at different target temperatures.

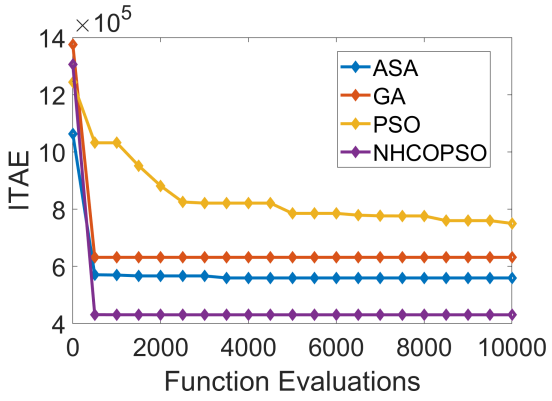

FIGURE 25. Convergence curves of ASA, GA, PSO, and NHCOPSO.

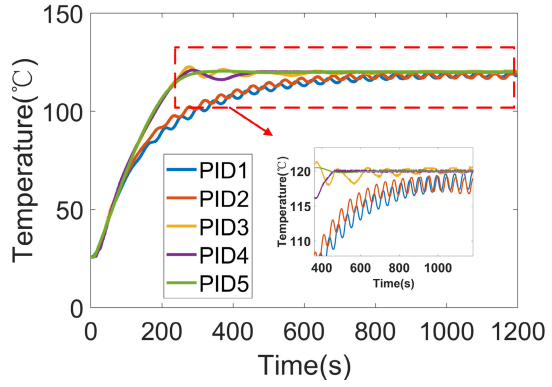

FIGURE 26. PID1–PID5 control curves during PID parameter optimization.

To better illustrate how NHCOPSO optimizes the PID parameters, Table 6 presents five sets of PID parameters derived during the iteration process, the corresponding control effect in terms of ITAE, and the *fitness* between the output curves of the LSTM network model and the actual model. On the other hand, comparing the PID control parameter optimization results shown in Table 5 and Table 6 when the target temperature is 120°C and 180°C, respectively, it can be demonstrated that the optimal control parameters in a temperature range are very similar, so segmented PID control method can be used. Fig. 26 shows the control curves corresponding to the five sets of parameters. Figs. 27–31 show the response curves of the LSTM network model and the actual temperature control system controlled by these five sets of PID parameters. The results verify that the LSTM network proposed in this paper accurately identifies the Peltier system.

VI. EXPERIMENTS AND COMPARISON

A. SYSTEM STRUCTURE

The test device, shown in Fig. 32, mainly includes an experimental gas flow control module, a circulating cooling device, the testing device, a power supply module, and a temperature control circuit board. The circuit board is connected with Peltier modules in the upper and lower plates of the cavity through the driving detection line, and

TABLE 5. Results of PID parameter optimization under the target temperature of 180°C.

Parameter	ASA	GA	PSO	NHCOPSO
K_p	211.7	183.5	863.9	210.0
K_i	11.2	4.5	11.9	4.6
K_d	1164.6	0	1354.7	236.7
ITAE	2.03E+06	2.29E+06	2.72E+06	1.56E+06

TABLE 6. PID parameters obtained during iteration process under the target temperature of 120°C.

Parameter	PID1	PID2	PID3	PID4	PID5
K_p	1422	1422	332.4	171.9	211.5
K_i	13.37	13.37	14.74	6.3	4.6
K_d	55.68	1093.4	1049.4	1093.4	184.5
ITAE	1306057	1263190	533451	455436	430700
Fitness/%	85.48	90.1	96.8	92.8	87.2

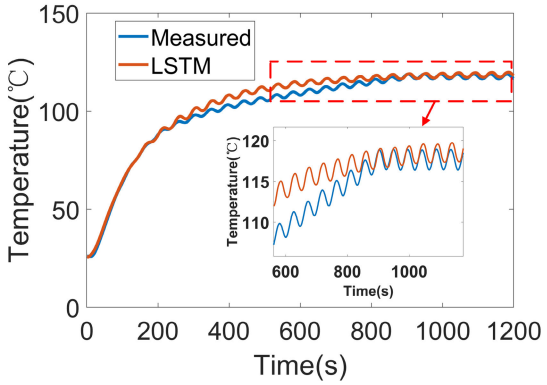

FIGURE 27. Comparison of the PID1 control curves between the LSTM network and the actual system (measured).

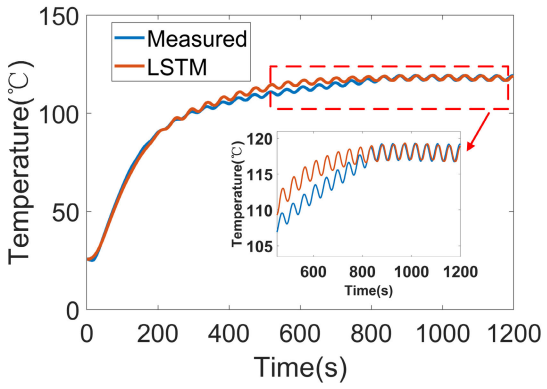

FIGURE 28. Comparison of the PID2 control curves between the LSTM network and the actual system (measured).

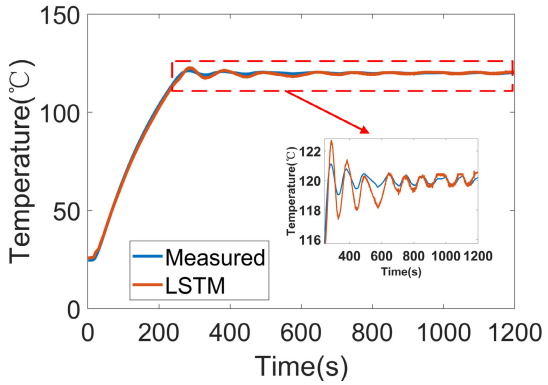

FIGURE 29. Comparison of the PID3 control curves between the LSTM network and the actual system (measured).

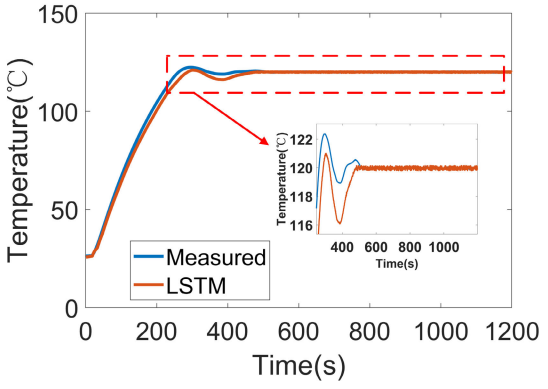

FIGURE 30. Comparison of the PID4 control curves between the LSTM network and the actual system (measured).

the temperature around the sensor is then adjusted by heat conduction. The Peltier module dissipates heat through the water/coolant circulation system. The cavity is opened or closed by lifting the upper plate. The upper and lower plates are served by experimental gas inlet and outlet channels, respectively, and the flow rate is controlled by the gas valve.

B. PERFORMANCE TEST OF THE TEMPERATURE CONTROL SYSTEM

Sections IV and V introduced the intelligent identification method for the Peltier temperature control system heating model based on an LSTM network and optimization of the PID control parameters at 120°C using NHCOPSO. The identification model for refrigeration temperature control can

TABLE 7. Parameters of piecewise PID control.

Parameter	$-40°C < T_{goal} < -20°C$	$-20°C < T_{goal} < T_r$	$T_r < T_{goal} < 90°C$	$90°C < T_{goal} < 180°C$
K_p	268.9	153.6	128.3	211.5
K_i	4.8	5.7	6.9	4.6
K_d	482.6	362.3	193.8	184.5
T_{op}(°C)	−30	0	60	120

TABLE 8. Performance of the temperature control system.

Parameter	Method 1 proposed in this paper	Method 2 used in references [5], [6], [7]
Heating method	Peltier	Blast heating
Cooling method	Peltier	Liquid nitrogen
Maximum heating rate	20°C/min	3°C/min
Maximum cooling rate	-10°C/min	-2°C/min
Temperature fluctuation	±0.05°C	±2.5°C
−40°C control time from room temperature	~17 min	>45 min
60°C control time from room temperature	~3 min	>15 min
180°C control time from room temperature	~18 min	>45 min

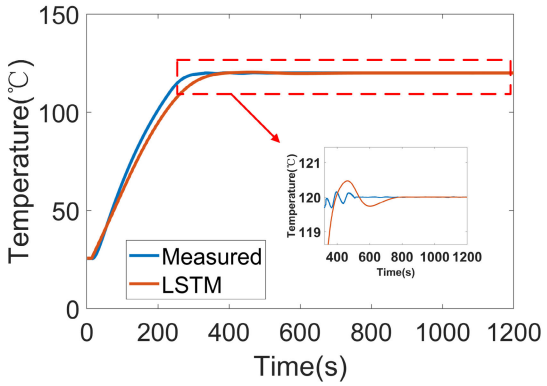

FIGURE 31. Comparison of the PID5 control curves between the LSTM network and the actual system (measured).

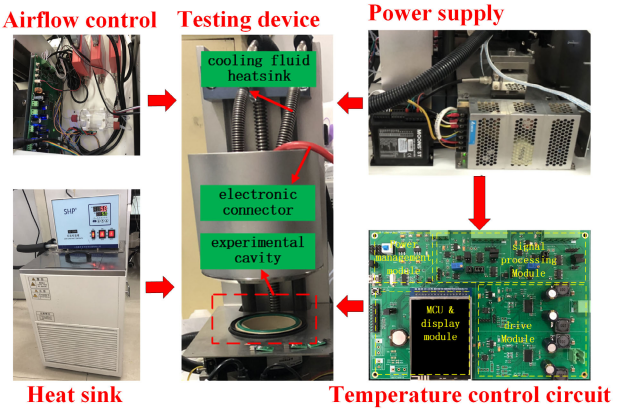

FIGURE 32. Structure of the test device, including the power supply, temperature control circuit board, heat sink, airflow control module, and testing device.

be obtained using the same method, and the optimal PID control parameters at various temperatures can be determined using NHCOPSO. Different target temperature values were divided into temperature ranges (see Table 7), and the corresponding PID parameters were used for temperature control. The temperature interval segmentation method is based on the optimization results for the control parameters under each temperature target. In Table 7, T_{goal} represents the current system target temperature, and T_r represents the current room temperature. The PID parameters of each temperature segment were obtained by PID parameter optimization at some temperature T_{op} close to the center of the temperature range.

This section considers five target temperature points, −40°C, 0°C, 60°C, 120°C, and 180°C, and examines the temperature control performance at each one. The temperature control curve is shown in Fig. 33. The experimental results show that the Peltier temperature control system allows the target temperature to be reached quickly and stably at high temperatures (120°C, 180°C), moderate temperatures (0°C, 60°C), and low temperatures (−40°C) and offers a good degree of temperature stability and control accuracy.

Table 8 compares the performance of the cantilever temperature control system designed in this paper (method 1) with the devices used in references [5], [6], and [7] (method 2). The performance of method 2 was measured with tests conducted at the Shanghai Institute of Microsystem and Information Technology, Chinese Academy of Sciences. It can be seen from the table that the heating and cooling speeds of method 1 are more than five times faster than those of method 2. The ambient temperature stability around the cantilever reaches ±0.05°C, and the heating/cooling times from

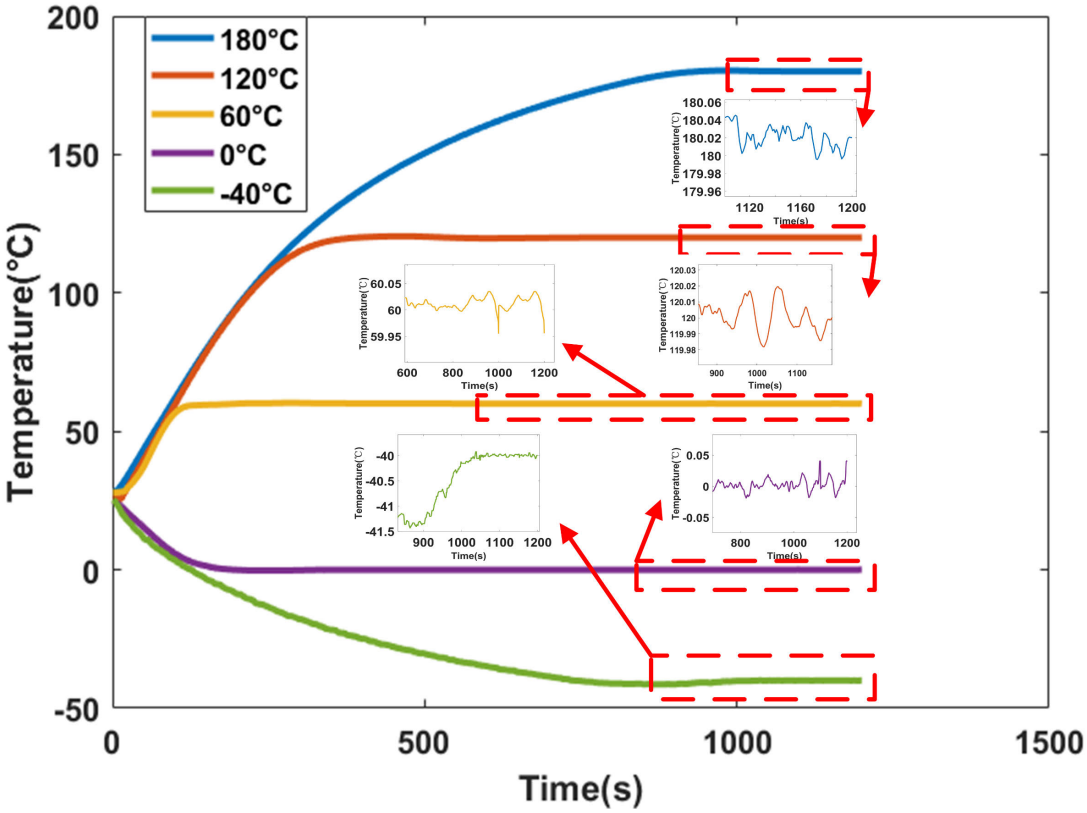

FIGURE 33. Temperature control curves with corresponding enlargements showing temperature stability at −40°C, 0°C, 60°C, 120°C, and 180°C.

room temperature to −40°C, 60°C, and 180°C are much shorter than when using method 2.

VII. CONCLUSION

This paper described a temperature control system for a cantilever-based analyzer to characterize gas-sensitive materials using Peltier elements, an LSTM network, and an improved PSO algorithm. First, the influence of environmental temperature control effects on material performance evaluation was analyzed. Based on the thermal model of semiconductor temperature control devices, an innovative cantilever temperature control device based on Peltier elements was proposed. Second, the nonlinear relationship between the input PWM duty cycle of the temperature control system and the temperature around the cantilever was established using an LSTM network. Finally, an improved PSO algorithm based on the neighborhood hybrid center and opposition-based learning was proposed. The NHCOPSO module offers better performance than other evolutionary algorithms on benchmark functions and for PID parameter optimization for the Peltier temperature control system. Experimental results show that the temperature control range of the Peltier system is −40 to 180°C, the stability is ±0.05°C, and the maximum heating/cooling speed is 20°C/min. Compared with traditional mechanical temperature control methods, this system can greatly reduce the size of the equipment required for gas-sensing material characterization. Furthermore, the proposed system improves the characterization accuracy, increases the heating/cooling speed, and simplifies the system integration process.

REFERENCES

[1] Y. Bao, P. Xu, S. Cai, H. Yu, and X. Li, "Detection of volatile-organic-compounds (VOCs) in solution using cantilever-based gas sensors," *Talanta*, vol. 182, pp. 148–155, May 2018.

[2] W. Li, M. Li, X. Wang, P. Xu, H. Yu, and X. Li, "An *in-situ* TEM microreactor for real-time nanomorphology & physicochemical parameters interrelated characterization," *Nano Today*, vol. 35, Dec. 2020, Art. no. 100932.

[3] L. Li, S. He, M. Liu, C. Zhang, and W. Chen, "Three-dimensional mesoporous graphene aerogel-supported SnO_2 nanocrystals for high-performance NO_2 gas sensing at low temperature," *Anal. Chem.*, vol. 87, no. 3, pp. 1638–1645, Feb. 2015.

[4] P. Xu, H. Yu, S. Guo, and X. Li, "Microgravimetric thermodynamic modeling for optimization of chemical sensing nanomaterials," *Anal. Chem.*, vol. 86, no. 9, pp. 4178–4187, May 2014.

[5] J. Ni, T. Zhao, L. Tang, P. Qiu, W. Jiang, L. Wang, P. Xu, and W. Luo, "Solution-phase synthesis of ordered mesoporous carbon as resonant-gravimetric sensing material for room-temperature H_2S detection," *Chin. Chem. Lett.*, vol. 31, no. 6, pp. 1680–1685, Jun. 2020.

[6] P. Xu, H. Yu, and X. Li, "Quantitatively extracted Gibbs free-energy (ΔG) as criterion to determine working temperature range of gas-sensing material," in *Proc. 18th Int. Conf. Solid-State Sensors, Actuat. Microsyst. (TRANSDUCERS)*, Anchorage, AK, USA, 2015, pp. 630–633.

[7] Y. Lv, H. Yu, P. Xu, J. Xu, and X. Li, "Metal organic framework of MOF-5 with hierarchical nanopores as micro-gravimetric sensing material for aniline detection," *Sens. Actuators B, Chem.*, vol. 256, pp. 639–647, Mar. 2018.

[8] A. Ihring, E. Kessler, U. Dillner, U. Schinkel, M. Kunze, and S. Billat, "A planar thin-film peltier cooler for the thermal management of a dew-point sensor system," *J. Microelectromech. Syst.*, vol. 24, no. 4, pp. 990–996, Aug. 2015.
[9] S. Yamaguchi and T. Anzai, "Impact of temperature dependence of resistivity on thermal time constant of direct-current-driven Peltier device," *Phys. Status Solidi C*, vol. 14, no. 5, 2017, Art. no. 1700118.
[10] K. K. Mahant, A. V. Patel, A. Vala, and R. Goswami, "FPGA based temperature control and monitoring system for X-ray measurement instrument," in *Proc. IEEE Region Conf. (TENCON)*, Singapore, Nov. 2016, pp. 3249–3252.
[11] A. Wassilkowska and T. Woźniakiewicz, "Application of Peltier cooling device in a variable-pressure SEM," *Solid State Phenomena*, vol. 231, pp. 139–144, Jun. 2015.
[12] M. Deng, A. Inoue, and S. Goto, "Operator based thermal control of an aluminum plate with a peltier device," in *Proc. 2nd Int. Conf. Innov. Comput., Inf. Control (ICICIC)*, Kumamoto, Japan, Sep. 2007, p. 319.
[13] H. Huang, S. Fu, P. Zhang, and L. Sun, "Design of a small temperature control system based on TEC," in *Proc. 9th Int. Symp. Comput. Intell. Design (ISCID)*, Hangzhou, China, Dec. 2016, pp. 193–196.
[14] G. Engelmann, M. Laumen, K. Oberdieck, and R. W. De Doncker, "Peltier module based temperature control system for power semiconductor characterization," in *Proc. IEEE Int. Power Electron. Motion Control Conf. (PEMC)*, Varna, Bulgaria, Sep. 2016, pp. 957–962.
[15] A. K. R. Sombra, F. C. Sampaio, R. P. T. Bascope, and B. C. Torrico, "Digital temperature control project using peltier modules to improve the maintenance of battery lifetime," in *Proc. 12th IEEE Int. Conf. Ind. Appl. (INDUSCON)*, Curitiba, Brazil, Nov. 2016, pp. 1–7.
[16] W. Lyskawinski and W. Szelag, "Analysis of cooling and heating system with Peltier cell," in *Proc. ITM Web Conf.*, vol. 19, 2018, Art. no. 01032.
[17] S. Kawahata and M.-C. Deng, "Operator-based nonlinear temperature control experiment for microreactor group actuated by peltier devices," *Int. J. Autom. Comput.*, vol. 13, no. 4, pp. 401–408, Aug. 2016.
[18] N. Wang, M. M. Chen, H. Z. Jia, T. Jin, and J. L. Xie, "Study of voltage-controlled characteristics for thermoelectric coolers," *J. Electron. Mater.*, vol. 46, no. 5, pp. 1–6, 2017.
[19] R. Sekiguchi, Y. Liu, and Y. Sano, "Thermal equivalent circuit of peltier device considered seebeck effect and driving method improving cooling efficiency of the device," *Electron. Commun. Jpn.*, vol. 101, no. 5, pp. 73–83, May 2018.
[20] Y. Guoqiang, L. Weiguang, and W. Hao, "Study of RBF neural network based on PSO algorithm in nonlinear system identification," in *Proc. 8th Int. Conf. Intell. Comput. Technol. Autom. (ICICTA)*, Nanchang, China, Jun. 2015, pp. 852–855.
[21] X. Gao, B. Sun, and S. Wang, "Hopfield neural network identification for Preisach hysteresis system," in *Proc. 37th Chin. Control Conf. (CCC)*, Wuhan, China, Jul. 2018, pp. 1580–1584.
[22] Q. Lv, Y. Zhang, and H. Lin, "A method of dynamic system identification based on memory RBF network," in *Proc. Chin. Control Decis. Conf. (CCDC)*, Yinchuan, China, May 2016, pp. 3051–3054.
[23] X. W. Zhang, "Temperature and humidity control system identification based on neural network in heating and drying system," *Appl. Mech. Mater.*, vol. 686, pp. 439–447, Oct. 2014.
[24] G. Wang, X. Yao, J. Cui, Y. Yan, J. Dai, and W. Zhao, "A novel piezoelectric hysteresis modeling method combining LSTM and NARX neural networks," *Modern Phys. Lett. B*, vol. 34, no. 28, Oct. 2020, Art. no. 2050306.
[25] R. Han, R. Wang, and G. Zeng, "Identification of dynamical systems using a broad neural network and particle swarm optimization," *IEEE Access*, vol. 8, pp. 132592–132602, 2020, doi: 10.1109/ACCESS.2020.3009982.
[26] S. S. Miriyala and K. Mitra, "Deep learning based system identification of industrial integrated grinding circuits," *Powder Technol.*, vol. 360, pp. 921–936, Jan. 2020.
[27] S. Wen, Y. Wang, Y. Tang, Y. Xu, P. Li, and T. Zhao, "Real-time identification of power fluctuations based on LSTM recurrent neural network: A case study on Singapore power system," *IEEE Trans. Ind. Informat.*, vol. 15, no. 9, pp. 5266–5275, Sep. 2019.
[28] N. Hirose and R. Tajima, "Modeling of rolling friction by recurrent neural network using LSTM," in *Proc. IEEE Int. Conf. Robot. Autom. (ICRA)*, Singapore, May 2017, pp. 6471–6478.
[29] Z. Wang, C. Li, X. Lai, N. Zhang, Y. Xu, and J. Hou, "An integrated start-up method for pumped storage units based on a novel artificial sheep algorithm," *Energies*, vol. 11, no. 1, Jan. 2018, Art. no. 151.
[30] T. Wu, C. Zhou, Z. Yan, H. Peng, and L. Wu, "Application of PID optimization control strategy based on particle swarm optimization (PSO) for battery charging system," *Int. J. Low-Carbon Technol.*, vol. 15, no. 4, pp. 528–535, Nov. 2020.
[31] N. I. M. Azmi, N. M. Yahya, H. J. Fu, and W. A. W. Yusoff, "Optimization of the PID-PD parameters of the overhead crane control system by using PSO algorithm," in *Proc. MATEC Web Conf.*, vol. 255, 2019, Art. no. 04001.
[32] H. Feng, C.-B. Yin, W.-W. Weng, W. Ma, J.-J. Zhou, W.-H. Jia, and Z.-L. Zhang, "Robotic excavator trajectory control using an improved GA based PID controller," *Mech. Syst. Signal Process.*, vol. 105, pp. 153–168, May 2018.
[33] Y. Qin, L. Sun, and Q. Hua, "Environmental health oriented optimal temperature control for refrigeration systems based on a fruit fly intelligent algorithm," *Int. J. Environ. Res. Public Health*, vol. 15, no. 12, Dec. 2018, Art. no. 2865.
[34] M. H. Sadafi, R. Hosseini, H. Safikhani, A. Bagheri, and M. J. Mahmoodabadi, "Multi-objective optimization of solar thermal energy storage using hybrid of particle swarm optimization and multiple crossover and mutation operator," *Int. J. Eng.*, vol. 24, no. 4, pp. 367–376, 2011.
[35] H. Sun, Z. Deng, J. Zhao, H. Wang, and H. Xie, "Hybrid mean center opposition-based learning particle swarm optimization," *Acta Electronica Sinica*, vol. 47, no. 9, pp. 1809–1818, 2019.
[36] L.-Y. Zhou, L.-X. Ding, H. Peng, and X.-L. Qiang, "Neighborhood centroid opposition-based particle swarm optimization," *Tien Tzu Hsueh Pao/Acta Electron. Sin.*, vol. 45, no. 11, pp. 2815–2824, 2017.
[37] I. B. Aydilek, "A hybrid firefly and particle swarm optimization algorithm for computationally expensive numerical problems," *Appl. Soft Comput.*, vol. 66, pp. 232–249, May 2018.
[38] M. Ghasemi, E. Akbari, A. Rahimnejad, S. E. Razavi, S. Ghavidel, and L. Li, "Phasor particle swarm optimization: A simple and efficient variant of PSO," *Soft Comput.*, vol. 23, no. 19, pp. 9701–9718, Oct. 2019.
[39] L. Zadeh, "From circuit theory to system theory," *Proc. IRE*, vol. 50, no. 5, pp. 856–865, May 1962.
[40] R. Pascanu, T. Mikolov, and Y. Bengio, "On the difficulty of training recurrent neural networks," 2012, *arXiv:1211.5063*. [Online]. Available: http://arxiv.org/abs/1211.5063
[41] D. P. Kingma and J. Ba, "Adam: A method for stochastic optimization," 2014, *arXiv:1412.6980*. [Online]. Available: http://arxiv.org/abs/1412.6980
[42] J.-H. Seo, C.-H. Im, C.-G. Heo, J.-K. Kim, H.-K. Jung, and C.-G. Lee, "Multimodal function optimization based on particle swarm optimization," *IEEE Trans. Magn.*, vol. 42, no. 4, pp. 1095–1098, Apr. 2006.
[43] H. R. Tizhoosh, "Opposition-based learning: A new scheme for machine intelligence," in *Proc. Int. Conf. Comput. Intell. Modeling, Control Autom. Int. Conf. Intell. Agents, Web Technol. Internet Commerce (CIMCA-IAWTIC)*, Vienna, Austria, 2005, pp. 695–701.
[44] J. Kennedy and R. Mendes, "Population structure and particle swarm performance," in *Proc. Congr. Evol. Comput. (CEC)*, Honolulu, HI, USA, vol. 2, 2002, pp. 1671–1676.

TIANHAI LU received the B.S. degree in electronic science and technology from Soochow University, China, in 2018, where he is currently pursuing the M.S. degree. His research interests include circuit system design and intelligent information processing.

CHAO FEI received the B.S. degree in electronic information science and technology from Nantong University, China, in 2018. He is currently pursuing the M.S. degree in electronics and communication engineering with Soochow University. His main research interests include information acquisition and intelligent processing technology.

LIN XUAN is currently pursuing the M.S. degree in electronic science and technology with the School of Electronic and Information Engineering, Soochow University, Suzhou, China. Her current research interest includes structure design and signal processing technology of MEMS sensors.

HAITAO YU received the B.S. degree in physics from Peking University, in 2004, and the Ph.D. degree in microelectronics and solid state electronics from the Shanghai Institute of Microsystem and Information Technology, Chinese Academy of Sciences, in 2009. He is currently a Professor with the State Key Laboratory of Transducer Technology, Shanghai Institute of Microsystem and Information Technology, Chinese Academy of Sciences. His current research interests include MEMS chemical sensors and lab-on-chip. Since 2017, he has been appointed as a member of the Youth Innovation Promotion Association CAS.

DACHENG XU received the B.S. degree in physics education from Northwest Normal University, Gansu, China, in 1984, and the M.S. degree in circuits and systems from the University of Electronic Science and Technology, Sichuan, China, in 1992. He was a Visiting Scholar with Twente University, Enschede, The Netherlands, and the National University of Singapore, Singapore. He is currently a Professor with the Department of Electronics and Information, Soochow University, Suzhou, China. His research interests include vibration energy harvester signal processing and MEMS inertial sensor circuit designing and measurement technology.

XINXIN LI received the B.S. degree from Tsinghua University and the Ph.D. degree from Fudan University. He worked as a Research Associate with the Hong Kong University of Science and Technology. He worked as a Research Fellow with Nanyang Technological University, Singapore. He joined Tohoku University, Japan, as a Lecturer (COE Fellowship). Since 2001, he has been a Professor. He has also worked as an Adjunct Professor with Fudan University, Shanghai Jiaotong University, Dalian University of Technology, Shanghai Tech University, and Suzhou University. From 2009 to 2013, he had worked as a Consultant Professor for World Class University Program of Korean with Chonnam National University, South Korea. He is currently working as the Director of the State Key Lab of Transducer Technology, Shanghai Institute of Microsystem and Information Technology, Chinese Academy of Sciences. He was granted the National Science Fund for Distinguished Young Scholar, in 2007. His Ph.D. student was awarded National Excellent 100 Ph.D. Dissertation, in 2009. He has invented about 100 patents and published more than 300 articles in refereed journals and conferences (including about 170 SCI journal articles). His research interests include micro/nano sensors and MEMS/NEMS. He ever served as TPC member for the conferences of the IEEE MEMS, Transducers, and IEEE Sensors. He is the Editorial Member of the *Journal of Micromechanics and Microengineering*. He is the International Steering Committee Member of Transducers.